Evaluating the Use of Seasonal Surface Displacements and Time-Variable Gravity to Constrain the Interior of Mars

N. L. Wagner[1], P. B. James[1], A. I. Ermakov[2], and M. M. Sori[3]

[1]Department of Geosciences, Baylor University, [2]Space Science Laboratory, University of California, Berkeley, [3]Department of Earth and Planetary Sciences, Purdue University

Corresponding author: Nick Wagner (nick_wagner2@baylor.edu)

Key Points:

- Global seasonal displacements of the surface of Mars are caused by the condensation and sublimation of CO_2 at the poles.
- We model the displacement caused by this change in mass and evaluate the needed measurement precision to constrain the interior of Mars.
- This reported displacement and gravity perturbation could be measured by a dedicated geodetic station or time-variable gravity mission.

Abstract

The mass transport of volatiles on Mars represents a seasonally changing load onto the lithosphere of the planet. Much like on Earth, as mass is redistributed across the planet, the surface responds in a complex manner becoming displaced downwards or upwards. The magnitude and extent of displacement depend on the properties of the load and mechanical properties of the planetary interior. Based on new estimates of the height variation of the seasonal polar cap (SPC) we predict local surface displacements of up to tens of millimeters with a strong degree 1 signal throughout the Martian year. The long-wavelength portion of the displacement is potentially observable, with a magnitude of a few millimeters, located away from the seasonal polar cap where we could realistically measure it with a landed or orbital mission. We also model the direct contribution of this process to observable time variable gravity where we find the odd zonal coefficients to be in line with previous measurements, although with a smaller magnitude. Future measurements of this displacement could be used to help elucidate the composition of the mantle and crust of Mars, using this process as a probe into the Martian interior. Furthermore, more refined measurements of time-variable gravity would be a powerful tool in constraining the pole-to-pole volatile cycle present on Mars.

Plain Language Summary

Mars has seasons that are similar to Earth's because of its axial tilt. This causes the CO_2 polar caps of Mars to grow and shrink depending on the time of year. This change in mass causes the lithosphere of Mars to physically displace downwards in response to the change in mass. The magnitude of this displacement is based upon the change in height of the polar caps and the interior properties of planets, as a more rigid planet would resist this displacement more. Using new estimates of the height variations we model what the magnitude and pattern of the displacement looks like across Mars. We find displacements of up to tens of millimeters at the poles and a few millimeters closer to the equator. We then evaluate the feasibility of measuring this displacement, and what we could do with that information if we collected it.

1 Introduction

Any redistribution of mass on a planetary body will cause a response from the interior. Variations in atmospheric mass have already been measured on numerous planetary bodies, with the response from the planetary interior being well characterized on Earth (Agnew, 2015). Atmospheric circulation and the seasonal deposition and sublimation of carbon dioxide on Mars represents one of the only current time variable processes that interacts with the interior of the planet. On Mars, the primarily carbon dioxide residual polar caps represent the largest sources of seasonal volatile mass transport on the planet. Like on Earth, these ice caps grow and shrink on an annual basis, extending a seasonal cap down to latitudes as low as 60° (Smith et al., 2001; Piqueux et al., 2015). As this is a seasonally dominated process, there will be sublimation of CO_2 ice and snow during the respective hemisphere's winter and spring and then condensation during the fall and winter, repeating annually. The SPCs represent a small portion of the entire mass budget of the polar layered deposits (PLDs), but is still significant enough to cause measurable changes in the gravity and shape of the planet (Smith et al., 2009).

The static deflection of the lithosphere from the permanent polar caps is debated as to its magnitude, depending on assumptions of the PLDs and how the deflection is calculated (Broquet et al., 2020, 2021; Ojha et al., 2019, 2021). Phillips et al. (2008) show that the lithospheric deflection underneath the northern polar layered deposit (NPLD) is no more than 100 meters, which implies an effective elastic thickness of 300 km or more, or that the response of the Martian interior to the load of the NPLD is still in a transient state. Because of variations in the dielectric properties of the ice caps, it has been difficult to determine this longer period static deflection of the lithosphere in addition to the mass balance of the PLDs. The time variable deflection of the lithosphere caused by the seasonal deposits may be easier to measure because it is a periodic signal. This is true although the seasonal displacements are far smaller in magnitude than the deflection caused by the weight of the underlying PLDs. We can observe this time variable displacement in real time far away from the portions of the surface covered by the perennial ice. The periodicity and predictability of this process makes it a reliable way to study its interaction with the lithosphere of Mars and extract thermal and compositional information about it. In addition to studies about the deflection of the lithosphere underneath the polar caps, there has also been work related to constraining their mass budget through gravity.

Through detecting temporal changes in the C_{20} and C_{30} gravity coefficients the amount of mass deposited and removed seasonally has been estimated to be on the order of 10^{15}kg (Karatekin et al., 2006; Lemoine et al., 2006; Smith et al., 2009; Konopliv et al., 2011; Genova et al., 2016) .Smith et. al. (2001), Aharonson et. al. (2004), and Xiao et al., (2022a) have constrained the topographic variation of the SPCs to change about one to two meters for the north pole and two to three meters for the south pole over the course of the year. With these constraints on the amount of mass and height of the topography variation, we can forward model the expected lithospheric deflection from this seasonal signal and deduce if this is detectable in current altimetry data. Xiao et al. (2022a) produced time variable maps of the height variations of each SPC and estimate the density of the deposits, allowing us to generate the expected deflection due to both the northern and southern SPC at different points in the Martian year. Furthermore, measuring the surface displacements caused by this seasonal loading would provide a needed constraint on the mechanical properties of the lithosphere of Mars, related to its thermal state and composition. The precision of these measurements is paramount to be able to differentiate between different interior models of Mars.

Previous studies have used estimates of this temporal change from GCMs to predict the solid body response (Métivier et al., 2008; Petricca et al., 2022), but here we use direct measurements of the height variations from dynamic MOLA profiles and static reference DTMs from self-registration of these laser altimetric tracks in order to predict the displacements (Xiao et al. (2022a) . These displacements then could be measured by a dedicated geodetic station or more sensitive orbital platform and then accounted for in height resolution analysis of the polar regions. For our modeling framework, we will use Load Love numbers (LLNs) to model the global displacements expected and evaluate the needed resolution of measured altimetry of this displacement in order to differentiate between different interior models of Mars. We will also evaluate the possibility of resolving these displacements with current data, as the displacements could be isolated in laser or radar altimetry or even be resolved in the current time variable gravity coefficients. Additionally, these new measurements of the height variation of the SPCs provides an avenue to benchmark estimations of the mass of the SPCs from gravity. Later in this paper we provide comparisons to previous mass estimates from gravity.

2 Methods and Data

2.1 Load Love Numbers

The history of solving surface mass loading problems on the Earth is long, as the basic theory was developed in the early 20th century and improved upon towards the end of the 20th century as computing capabilities grew (Love, 1906, 1911; Takeuchi, 1950; Longman, 1963; Farrell, 1972). Love numbers are dimensionless coefficients that characterize the response of a planetary body to forcing. Generally, k is the love number associated with the induced potential variation, h is associated with the vertical, or radial, displacement, and l is associated with the lateral, or tangential, displacement. LLNs thus characterize a planetary body's response to surface loads. Tidal Love numbers are denoted by k, h, and l, LLNs are denoted by k', h', and l', and finally shear Love numbers are denoted by k'', h'', and l''. We use the software package LoadDEF (Martens et al., 2019) to calculate the LLNs and evaluate the displacements in the spherical harmonic domain using SHTools (Wieczorek & Meschede, 2018) with the height variations from Xiao et al. (2022a). LoadDEF solves for the LLNs assuming a spherically symmetric, nonrotating, elastic, and isotropic body. The LLN that characterizes vertical displacement, h'_n, is computed by integrating the equations of motion for deflection on a sphere of an elastic, self-gravitating, and hydrostatic body. Thus, h'_n is highly sensitive to the interior elastic profile of a planet. Once we have our LLNs from LoadDef, we use equation 1, modified from Rietbroek et al. (2014), Agnew (2015), and Wieczorek (2015), to relate them to vertical, more thoroughly defined as radial, displacements.

$$\delta r(\theta,\lambda) = \frac{3\rho_{load}}{\bar{\rho}} \sum_{n=0}^{nmax} \sum_{m=0}^{n} \frac{h'_{nm}}{2n+1} H_{nm} \bar{Y}_{nm}(\theta,\lambda) \tag{1}$$

$\bar{\rho}$ is the average density of the planet, H_{nm} is spherical harmonic expansion of the height of the surface mass variation, and ρ_{load} is the density of loading material. H_{nm} is related to $H(\theta,\lambda)$ through:

$$H(\theta,\lambda) = \sum_{n=0}^{nmax} \sum_{m=0}^{n} H_{nm} \bar{Y}_{nm}(\theta,\lambda) \tag{2}$$

θ and λ represent the longitude and latitude of the observation position on the surface of a planet. Additionally, $\bar{Y}_{nm}(\theta, \lambda)$ are the fully normalized spherical harmonic functions and *nmax* is the max spherical harmonic degree that the function is expanded to. The radial displacement at the equator is not as large as the N-S displacement at the same location due to the large degree-1 translation. Thus, we also consider the full vector displacement at an equatorial station, such as InSight. We define the north-south and east-west displacements in equation 3:

$$\delta e(\theta, \lambda) = \frac{3\rho_{load}}{\bar{\rho}} \sum_{n=0}^{nmax} \sum_{m=0}^{n} \frac{l'_{nm}}{2n+1} H_{nm} \frac{\partial \bar{Y}_{nm}(\theta, \lambda)}{\sin\theta \, \partial\lambda}$$

$$\delta n(\theta, \lambda) = \frac{-3\rho_{load}}{\bar{\rho}} \sum_{n=0}^{nmax} \sum_{m=0}^{n} \frac{l'_{nm}}{2n+1} H_{nm} \frac{\partial \bar{Y}_{nm}(\theta, \lambda)}{\partial\theta} \tag{3}$$

Although a subscript of n and m imply that this spherical harmonic field varies over both degree and order, we assume that the LLNs are only degree dependent and do not vary with order (i.e., $h'_{20} = h'_{21} = h'_{22}$). For our LLNS, we used three interior models of Mars: one from a geodynamic inversion (MD; Samuel et al., 2019; Drilleau et al., 2021), one from a geophysical inversion (AK; Khan et al., 2018), and one from a seismic inversion (CD; Stähler et al., 2021). The geodynamically parameterized model considers quantities that influenced the thermochemical evolution of the planet. The geophysically parameterized model reflects a unified description of phase equilibria, seismic properties, and thermochemical parameters. Lastly, the seismically constrained model considers a layered model of Mars, without use of geodetic data, that describes velocity gradients of P- and S-waves. Values of density and seismic wave velocity varied slightly from model to model, as well as the radius of the mantle and core. In essence, the models reflect our current understanding of the interior of Mars given varying degrees of freedom. Figure 1 shows the properties of each model as a function of depth. Additionally, the shaded in regions show models between the 5th and 95th confidence intervals of the models. Ideally, measurements of lithospheric deflection from seasonal volatile transport would help differentiate between the interior models used by way of an inverse problem, and thus the precision of measurement needed to differentiate the model is also considered and discussed. The construction of the full inverse problem, however, is outside the scope of this study. In Figure 2 we also show systematic perturbations to the mechanical properties of planet to conduct a sensitivity analysis of the displacements to each separate parameter. We perturb these values by 10% both negatively and positively with respect to the median profile. For the LLNs LoadDef has the capability to calculate them for differing loading periods, and thus we set the frequency of forcing to be a full Martian year. This loading period is incorporated into the inertial terms in the equations of motion used to solve for the LLNs.

Figure 1: Depth profiles of each interior model used. The color region indicates the 5th and 95th percentile of interior profile in the suite of models used. The dashed lines indicate the median interior model. There are 100 subsets of each model type for a total of 300 total models considered in this study. AK (blue) represents the geophysical inversion, MD (red) represents the geodynamic inversion, and CD (green) represents the seismic inversion. Subplots A,B, and E

represent vp, vs, and density from the interior models supplied. C and D are the shear and bulk modulus, respectively, and are shown in common log space.

It should be noted that interior models for Mars include a liquid core. One of the assumptions that LoadDEF runs on is that the inner and outermost layers of the planet are solid. We set the inner kilometer of Mars to be solid in order to meet this assumption, however, this should not affect our results as the magnitude of the displacements expected are not significantly sensitive to the inner core (Martens et al., 2016, 2019). Additionally, the assumption of a spherically symmetric body is valid as loading displacements are not significantly sensitive to lateral topography variations, the largest of which on Mars is the hemispheric dichotomy (Métivier et al., 2008). We test changes in the displacement with different assumptions of topographic and crustal variations using a finite-element model and further justify this choice. We include these results and discussion in S1.

Figure 2: Depth profiles of each perturbed interior model used. We have only perturbed the properties within the mantle and thus only show the mantle in these plots. The smaller dashed lines indicate the perturbation of each mechanical property -10% and +10% of the median value of the interior profile in the suite of models used. AK (blue) represents the geophysical inversion, MD (red) represents the geodynamic inversion, and CD (green) represents the seismic inversion. The shear and bulk modulus are shown in common log space.

2.2 Treatment of Degree 1

The seasonal transport of volatiles not only causes elastic deformation of the solid Mars, but also changes the center of figure of the Mars system. The center of mass of the Mars-Sun system will be conserved, but Mars will oscillate north and south about a point in its interior as the mass moves from pole to pole. In essence, this is a degree one translation that needs to be considered when evaluating the displacements. The center of mass frame includes this degree one translation, so we will be evaluating and analyzing the center of mass results as in practice this degree one translation would be observable. The conversion to a center of mass reference frame is easy and defined by equation 4 (Blewitt, 2003).

$$[h'_1]_{CM} = [h'_1]_{CE} - 1 \tag{4}$$

Figure 3 shows, in a center of mass fixed frame, how the center of figure of Mars moves in response to the redistribution of mass. We only consider this for the height displacements, as the origin of the gravity field coincides with the center of mass of the planet (Blewitt, 2003; Petricca et al., 2022).

Figure 3: A schematic representation of the center of figure moves in response to the redistribution of mass. We plot this for a visualization of the large degree 1 signal seen in our results. However, when considering residuals between models, this degree 1 translation cancels out, as it is controlled by the amount of mass in the load, which we consider constant. The red star represents the COF before loading, and the blue square represents the COF after loading. Schematic not to scale.

2.3 Height Variations

The height variation data used in this work is sourced from Xiao et. al. (2022b) and Xiao et. al. (2022c). They estimated the precision of height variations of the polar caps to be around 4–5 cm, depending on the location, which represents an improvement compared to previous precisions of 10–20 cm (Smith et al., 2001; Aharonson et al., 2004). In addition to time variable height measurements, they also retrieved estimates of the density of the snow as a function of time with an energy balance model. The height variations are derived from MY24 into MY25, so approximately a little more than one Martian year. In our loading procedure, we take the density of the load to be those found by both Xiao et. al. (2022b) and Xiao et. al. (2022c) with the density outside the given range found by them to be 0 as the measurement becomes biased and is unreliable. One implicit assumption of this study is that the height variations measured in these studies and the resulting deflection are still convolved with each other. Thus, the height variations used are likely an upper bound on the height variations of the SPCs as the surface deflection would contribute to the height changes measured by MOLA. Future coeval consideration of both these height changes would need to be considered to deconvolve their contribution to the total observed displacement.

3 Results

3.1 LLNs

We calculated the LLNs for the range of interior models available to us. Figure 4 reports the values of the LLN's calculated for the range of interior models considered. Plotted are the degree dependent Love numbers of both the change to the surface height ($\boldsymbol{h'}$) and the potential ($\boldsymbol{k'}$). We include a plot of *l'* in S2. We also include the results from Petricca et al. (2022) for comparison. *h'* is highly sensitive to the interior model used whereas k' is less sensitive. As expected, the LLNs produced with the seismically inverted model, which had the highest variability between the three models, varied the most. The results from Petricca et al. (2022) are

Figure 4: LLNs h' and k' plotted as a function of spherical harmonic degree. The different colors and tick shapes indicate the interior model used in calculating the respective Love Number. The color region indicates the 5^th^ and 95^th^ percentile of interior models from Figure 1.

also similar to ours, even though they had calculated viscoelastic LLNs. However, although k' is extremely similar, there seems to be a departure between our calculated h' values. The shape of the curves is similar but is higher in magnitude. The model that Petricca et al. (2022) used that best matched our LLNs results used a lower reference viscosity in the mantle of 10^{19} Pa s. Although not plotted, our results are also like those of Métivier et al. (2008), despite them varying in magnitude. Our lower degree h' values are higher in magnitude than in Métivier et al. (2008) but towards higher degrees match better. Our k' values show much similarity with those found in Métivier et al. (2008), continuing the trend seen with comparing our results with Petricca et al. (2022). Plotting the minimum and maximum LLN values of each model also shows that the uncertainty in interior model leads to vertical shifts in these curves. Essentially only changing the magnitude of the response and not the shape of the curve at varying spherical harmonic degrees. Figure 5 shows the LLNs calculated for the systematic perturbations to the mechanical properties of the interior with respect to the median profile.

Figure 5: LLNs h' and k' plotted as a function of spherical harmonic degree. The different colors and tick shapes indicate the interior model used in calculating the respective Love Number. The dotted line indicates the -10% perturbed model and the dashed line indicates the +10% perturbed model. Perturbed models are calculated from the median profile shown in figure 1.

3.2 Radial Surface Displacements

3.2.1 Temporal Dependence

Figure 6:Radial surface displacements at different times in the Martian year given the AK model. Each row represents a different season and each column represents the displacements from the 5th percentile, 95th percentile, and median interior profiles. These plots are shown in the COM reference frame. Negative is inward radial.

Figure 6 shows the global radial displacement field for three evenly spaced values of solar longitude. Radial displacements that result from seasonal volatile loading are of order millimeters to centimeters. These displacements scale with the height of the residual cap, with the displacements in the southern hemisphere being nearly twice the magnitude of those in the northern hemisphere, mirroring the difference in height variations between the two poles. There is a strong degree one signal present due to the center of figure translating relative to the center of mass. The magnitude seen in the winter affected hemisphere is slightly more than the opposite one. This is because of the combination of the elastic displacement of the surface of Mars with the reference frame translation. Between the 5th percentile mode, 95th percentile model, and the median there is some difference in the magnitude of the displacement. As the 5th percentile model provides the highest displacement with the 95th percentile and median models being more similar.

3.2.2 Model Dependence

In addition to the temporal dependence of surface displacements, there will also be dependence upon the mechanical properties of the interior. Figure 7 shows an example of how

Figure 7: Radial displacement as a function of interior model. Each row shows the displacement for one time slice, two models, and the difference between the two models. The chosen time is Ls = 190. These plots were created using the median values for the interior model and shown in COM reference frame. Negative is inward radial.

the residual difference between displacement based upon a certain interior profile will vary. The seismically derived model (CD) was the model which varied the most, and we can see how the difference between the surface displacements given that interior model is the highest. Quantitatively speaking, to be able to measure these displacements the precision of a measurement must be on the order of millimeters. Further still to be able to differentiate between interior models reliably and confidently an instrument would need precision on the millimeter to sub-millimeter scale. These plots highlight the need for high resolution in the measurement of these displacements, as the differences in the established and accepted models do not translate to substantially large differences in displacement. There is also spatial dependence, as the SPC height variations are not latitudinally constant, and thus offer a way to study any laterally variable properties of the interior. Most notably, the displacement across the entire planet is still within measurable bounds. Equatorial displacements are still on the order of millimeters, meaning that current landed instrumentation, InSight for instance, could theoretically resolve this displacement. The optimum location to observe these displacements is likely anywhere lower in latitude than the edge of the snow line. If an instrument would be placed above the snow line, then one would also have to consider the effect of accumulating ice on the height resolution. This snow line is roughly 60°N and 60°S and represents where there is no seasonal snow or ice.

3.2.3 Sensitivity Analysis

In

Figure 8: Global displacement plots that show the difference between the -10% and +10% perturbed, with respect to the median model, models given by the interior models in figure 2. Displacements shown in the center of mass reference frame. Negative is inward radial.

addition to evaluating LLNs and displacements from the full range of models presented, we also conducted a sensitivity analysis to systematic perturbations to the mechanical properties of the mantle. We perturbed ρ, μ, and κ individually by +10% and -10% and evaluated the difference in LLNs and surface displacements. We also considered a model where all three properties were perturbed together. Figure 8 shows these differences. We see that the perturbations to density result in the largest variations in surface displacement, followed by perturbing all three, μ, and finally κ. Any measurement of the surface displacement would thus be sensitive to these parameters in this order, as a change to density, for instance, would change the magnitude of the displacement more than a similar change to the elastic moduli. However, when we perturb all three variables we see that the change in density causes a larger magnitude change in the displacement than the elastic moduli because of linearities. Thus, the displacement is most sensitive to changes in the density.

3.5 Gravity Perturbation

Gravity has been used to constrain the mass of both SPCs and below we expand the new results found by Xiao et al., (2022b) and Xiao et al., (2022c) to compare with previous gravity studies. The curves shown in figure 9 are found from calculating the gravitational anomaly caused by the height variations, using the density and heights we used in the displacement calculations. We do not show the gravity from the displacement of the crust because it is about an order of magnitude lower than the signal from the deposits themselves.

Figure 9: Normalized zonal coefficient terms of the spherical harmonic expansion of the change in the gravity expected from the modeled load. The dotted red lines are the fitted zonal curves reproduced from Smith et al. (2009), Konopliv et al. (2011), and Genova et al. (2016). Values are subtracted by the average to look at relative changes from the mean.

The shape of our curves slightly differs than previous results, mainly seen in the difference in magnitude at the maximum extent of the NSPC and SSPC. The shape of $\bar{\boldsymbol{C}}_{\mathbf{20}}$ is matched most closely by the results of Genova et al. (2016), whereas the shape of $\bar{\boldsymbol{C}}_{\mathbf{30}}$ is matched equally well by each previous study. Futher, our results specifically match the $\overline{\boldsymbol{C}}_{\boldsymbol{20}}$ result from Genova et al. (2016) that only use the tracking data from Mars Odyssey and not MGS or MRO. As processing technqiues have improved we can see that our estimate of $\overline{\boldsymbol{C}}_{\boldsymbol{20}}$ is matched better from Smith et al. (2009) to Genova et al. (2016). The departure in magnitudes at the peak of each of these curves is likely from one of two sources. The first is that the height variations, or density, reported by Xiao et al. is lower than it actually is. The second is that, even though these previous coefficient estimates have corrected for atmospheric effects, there might be unmodeled mass redistribtution effects from dust and the non-volatile portion of the atmosphere that measured gravity would be sensistive to and overestimate the contribution from the SPCs. Thus, our $\overline{\boldsymbol{C}}_{\boldsymbol{20}}$ curves are what would be expected for a changing atmosphere where the only time variable contribution is from the SPCs. We also use C_{20} and C_{30} to estimate the magnitude of the mass being transported by this process. This mass is calculated by treating it as a point mass as defined by equation 5:

$$\boldsymbol{M}_{\boldsymbol{NSPC}} = \frac{\boldsymbol{C}_{\boldsymbol{20}}+\boldsymbol{C}_{\boldsymbol{30}}}{\boldsymbol{2}}\boldsymbol{M}_{\boldsymbol{Mars}}$$

$$\boldsymbol{M}_{\boldsymbol{SSPC}} = \frac{\boldsymbol{C}_{\boldsymbol{20}}-\boldsymbol{C}_{\boldsymbol{30}}}{\boldsymbol{2}}\boldsymbol{M}_{\boldsymbol{Mars}} \tag{5}$$

Where $\boldsymbol{M}_{\boldsymbol{Mars}}$ is the mass of Mars (Genova et al., 2016; Karatekin et al., 2006; Lemoine et al., 2006). This method provides a good estimate of the mass of each SPC. However, because we have access to measured height variations as a function of latitude and longitude, we can also directly compute the volume and mass of the SPC. Figure 10 shows our derived curves for the mass of the northern and the southern SPC using both the estimation method and the direct calculation.

Figure 10: Mass estimates of the NSPC and SSPC from the derived C20 and C30 gravitational potential terms (estimate) and summed volumes of the height variations (direct). We also include results from Karatekin et al. (2009), Smith et al. (2009), and Genova et al. (2016) for comparison.

Our estimates of mass are roughly the same shape and but slightly lower in magnitude than the ones derived by previous studies. There is good agreement with the location the peaks of both polar caps. Likely, as stated before, this magnitude difference could be due from unmodeled mass variations in the atmosphere, such as dust. It could also be due to an underestimation of either the density or height variations of the SPC. The direct result is also slightly larger than the estimation, which is due to the mass not being entirely concentrated at the poles. This breaks the assumption that the C_{20} and C_{30} estimation assumes. Compared to other estimates other than from Genova et al. (2016) we can see our results are closer to the estimates from Karatekin et al. (2009) and Smith et al (2009). Conveniently Smith et al. (2009) also directly estimated the mass of the atmosphere, and thus we also included it in this plot to show how each three of these volatile resovoirs trade off mass depending on the time of year.

3.6 Tidal Displacements

In addition to the displacements induced by surface loading, there are also displacements caused by solar and satellite tides. In Mars' case the largest contributors to this tidal displacement are the Sun and Phobos. The tidal potential of Deimos is negligible (Van Hoolst et al., 2003). Using tidal potential theory and ephemeris' from SPICE kernals we calculate the expected deflection caused by the tidal potential of the Sun and Phobos in order to provide bounds on the expected displacement that would actually be observed on the surface of Mars (C. Acton et al., 2018; C. H. Acton, 1996; McCarthy & Petit, 2003). Once we calculate the tidal potential of the perturbing bodies we multiply it by the tidal Love Number h_{nm}, also produced by LoadDEF (Asmar et al., 2014; McCarthy & Petit, 2003). We modified and corrected the equations given by Asmar et al. (2014) for our calculation of the fully normalized degree two tidal displacements. The radial displacements, defined in spherical harmonics coefficients, are given by equation 6.

$$\Delta\bar{C}_{20}^{r} = h_{20}\sqrt{\frac{1}{5}\frac{GM_pR^4}{GMr_p^3}}\left[\frac{3}{2}\sin^2\varphi_p - \frac{1}{2}\right]$$

$$\Delta\bar{C}_{21}^{r} = h_{21}\sqrt{\frac{3}{5}\frac{GM_pR^4}{GMr_p^3}}\sin\varphi_p\cos\varphi_p\cos\lambda_p$$

$$\Delta\bar{S}_{21}^{r} = h_{21}\sqrt{\frac{3}{5}\frac{GM_pR^4}{GMr_p^3}}\sin\varphi_p\cos\varphi_p\sin\lambda_p$$

$$\Delta\bar{C}_{22}^{r} = h_{22}\sqrt{\frac{3}{20}\frac{GM_pR^4}{GMr_p^3}}\cos^2\varphi_p\cos 2\lambda_p$$

$$\Delta\bar{S}_{22}^{r} = h_{22}\sqrt{\frac{3}{20}\frac{GM_pR^4}{GMr_p^3}}\cos^2\varphi_p\sin 2\lambda_p \quad (6)$$

φ_p and λ_p are the latitude and longitude of the perturbing body on the central body. M_p and r_p are the mass and radial distance of the perturber. M and R are the mass and radius of the central body, which is Mars in this case. We only use the degree two term of the tidal potential for both bodies because higher order terms are negligible for surface displacements. Therefore, we also only use the degree two tidal Love number. We assume the Love numbers for each order are equal ($h_{20} = h_{21} = h_{22}$). To find the total displacement from tides we take the coefficients in equation 6 and insert them into equation 7:

$$\delta r_{tides}(\theta, \lambda) = \sum_{m=0}^{2} (\bar{C}_{2m}^{r} \cos m\lambda + \bar{S}_{2m}^{r} \sin m\lambda) \bar{P}_{2m}(\sin \phi) \tag{7}$$

Figure 11: Maximum and minimum radial surface displacement from the combined tidal potential of the sun and Phobos. The maximum and minimum was evaluated over a Martian year. This plot represents the contribution, or potential error, induced by tidal displacements at any given point in a Martian year and time of day. This plot also includes a permanent tide correction.

We use estimates of this tidal displacement to place upper and lower bounds on the measured displacement from a theoretical geodetic station. The magnitude of these displacements is smaller than those induced by the SPCs but is the same order of magnitude as the residual between models. Figure 11 shows upper and lower bounds globally for tidal displacements from the combination of Phobos and the Sun. We only included tidal Love Numbers for models AK and MD as CD did not provide a stable solution. As these are just elastic estimates, more comprehensive tidal modeling must be conducted to characterize the frequency dependence more thoroughly on solid body tides to separate this displacement from surface loading displacements (Bagheri et al., 2019; Bagheri et al., 2022). We provide these estimates as upper bounds for the total magnitude of the degree two tidal displacement from Phobos and the Sun. Additionally, the difference in tidal displacements assuming different interior models is so small that measuring the solid body tide alone may not be as useful as additionally measuring the surface load displacements for characterizing the interior properties of Mars.

4 Discussion

4.1 Love Numbers

Two other studies have evaluated the LLNs for Mars. Métivier et. al. (2008) evaluated LLNs for models of Mars that varied the phase state of the core, the depth to the core-mantle boundary, and the crust-mantle boundary. Petricca et al., (2022) also did this and introduced a more sophisticated rheology, varying the viscosity of the mantle and core size. Comparing our $\boldsymbol{h'}$ and $\boldsymbol{k'}$ to Métivier et. al. (2008) we can see our values are much different; this is likely due to the added complexity in the interior models we used in this study and further knowledge about the interior of Mars. Models that have a larger and liquid core match our LLNs better, which is to be expected. The shape of our $\boldsymbol{h'}$ values match well to Petricca et. al. (2022), however ours are larger in magnitude for nearly all models. This difference is likely due to the addition of rheologic complexity in their models, notably the addition of viscoelastic layers which modulates the magnitude and phase lag of the displacements observed. Thus, any measurement of the LLNs would provide an immediate constraint on the magnitude of displacement and thus the rheologic dissipative conditions of the interior of Mars. Indeed, figures 4 and 5 show us how valuable measurements of $\boldsymbol{h'}$ concurrently with $\boldsymbol{k'}$ would be in investigating Mars' interior. As noted by Petricca et. al. (2022), dual use of measurements of $\boldsymbol{k'}$ and k can further extend the scientific return of a geodetic mission. One way to directly measure $\boldsymbol{k'}$ would be to employ an orbital mission with dedicated gravity observations, like the GRACE and GRAIL missions at the Earth and Moon, to Mars to measure the time variable contributions to the gravity field and evaluate how the SPC's contribute to this signal. Previous studies have evaluated this with MRO, MGS, and Odyssey measurements and our results are somewhat similar (Genova et al., 2016). However, a dedicated mission to measure $\boldsymbol{k'}$ would be extremely useful in modeling the dynamic interaction between atmospheric forcing and the interior of Mars.

4.2 Uncertainties

The uncertainty in the height variations used in this study, are at best, an order of magnitude better than previous published results. Xiao et. al. (2022a) reports uncertainties ranging from 2cm to as high as 30cm with a majority between 5–10cm, depending on location. Smith et. al. (2001) and Aharonson et. al. (2004) previously reported uncertainties in height measurements to be 25–30cm. We refer the reader to Xiao et. al. (2022a) for their height precision maps and how they change as a function of both latitude and longitude. This new precision is a great improvement; however, this uncertainty is still larger than the surface displacements presented in this study. Thus, any prospects, as of the writing of this paper, in resolving the surface displacements using MOLA altimetry are unrealistic. There are other prospects, however, in using future mission data to detect these displacements (see discussion in Section 4.3).

There is coeval displacement with the addition of a tidal perturbation. Tidal displacements are largely latitudinally constant if we considered an entire Martian year, and thus, contribute to the displacement at any given point on the Martian surface. As seen in Figure 11, we have plotted upper and lower bounds on the tidal displacement of the combined effect the sun and Phobos have on the surface of Mars. This confounding tidal signal is on the same order of magnitude as the height variation induced by loading. In some cases, this value eclipses the difference between modelled interior models and thus is important to consider, especially when resolving displacements closer to the equator where tidal displacements get larger and loaded displacements get smaller. Any measured displacement value should be corrected for the tidal displacement induced at the time of measurement. We only considered elastic displacements in the scope of this study and thus any practical attempt to remove the tidal signal would need to model the displacements more thoroughly with a viscoelastic rheology (Bagheri et al., 2019).

One last issue to consider is the convolution between the height variation measurements and the displacement. Without correcting for the displacement, the measured height variation will include the displacement in the measurement. The opposite is true of course but because we have measurements of the height variations and not the displacement, thus this is the most obvious one to discuss. For future height variation measurements, this displacement must be considered to both provide more accurate height variation data and to tighten the uncertainty in induced displacement.

4.3 Implications for Landed and Orbital Missions

The InSight mission is equipped with a ranging instrument (RISE) that acts as a geodetic station and thus has some sensitivity to surface displacements. Figure 12 shows what these radial displacements would look like at the location of InSight, given the range of the three interior models.

Figure 12: The expected radial, or vertical, E-W, and N-S displacement at the location of InSight. We refer the reader to the web version of the article as it is hard to differentiate the AK and MD curves without color. The color region indicates the displacement based on the 5th and 95th percentile interior model.

Unfortunately, this magnitude of a tens of millimeters, at best, is too small for the RISE instrument to detect (on the order of tens of meters), and the period is too long for the seismometer to detect (a few hundred seconds) (Folkner et al., 2018; Le Maistre et al., 2023; Mimoun et al., 2017). A future geodetic mission should have these considerations in mind to be able to measure the displacement modeled in this study. Perhaps more important than the radial displacement is the north-south displacement, which has a magnitude of ~6 centimeters at its peak. A future geodetic mission should thus be sensitive to the vector displacement and not just any one single component. InSight does indeed have a retroreflector that could be used as a ranging station (Porcelli et al., 2019). Various line of sight measurements from Earth during different times of day and year could be used to tease out each vector component. Future work should be conducted in leveraging this instrument as the principle of detecting surface displacements from tides with laser altimetry has been demonstrated on the Moon and theorized for Mercury and Ganymede (Briaud et al., 2023; Steinbrügge et al., 2015; Williams et al., 2001, 2006).

Across all three interior models considered, the maximum displacement predicted is on the order of a few centimeters (Figure 6 & 7). However, this maximum displacement is seen at the poles, underneath the SPCs, where it would be difficult to observe. To be able to reliably measure any periodic displacement with a landed geodetic station, one would need to measure the displacement out and away from the cover of the SPCs and the seasonal snow, which can extend down as equatorward as 60°. The expected deflection is an order of magnitude lower here (millimeters instead of centimeters), but still within realistic bounds of measurement. Considering that the magnitude of tidal displacements from the combined effect of Phobos and the Sun are the same as this displacement, proper consideration, and modeling of these tidal effects at the time of a geodetic measurement would be essential. Likely, the resolution would need to be an order of magnitude lower than this level to differentiate between interior models and tighten uncertainties in the interior properties. Our modeling efforts only consider the elastic response of the lithosphere. There would be a viscoelastic lag of when the load is applied associated with the timescale of the response of the lithosphere and dissipative properties of the mantle and crust. This viscoelastic response of Mars needs to be considered and constrained more thoroughly to determine how long this lag would be and if off-season displacements are from loads applied seconds, hours, days, or weeks prior.

Interferometric synthetic aperture radar (InSAR) could be a potential avenue to investigate this time-variable displacement from orbit. The sensitivity of Earth-based satellites is precise enough to measure ground deformation from a variety of processes. New, precise gravity measurements from orbital spacecraft at Mars would additionally be useful (e.g., Sori et al., 2022; Sori et al., 2023). The temporal evolution of the polar caps is inherently tied to the time-variable gravity of the planet, and both must be considered and measured to tighten constraints on models of Mars' interior. As seen in our LLN calculations, $\boldsymbol{k'}$ doesn't vary as much as $\boldsymbol{h'}$ does given accepted interior models, and thus being able to constrain $\boldsymbol{h'}$ would allow us to also constrain *k'*. This point highlights the importance of dual measurement of displacements with time-variable gravity. The interplay between the two can elucidate more information about the interior state than just one measurement on its own.

One consequence of this process that has not been considered in previous studies is the effect of this surface displacement on the measurement of the height variations of the SPCs. The magnitude of the displacement is an order of magnitude smaller than the current precision of the height variations, however, it will still be convolved with the measured value for future studies that investigate the height variations of the SPCs. For maximum precision, they must be corrected for while resolving the height variations. Thus, without correcting for these displacements, height variations have been slightly overestimated up until this point. In practice, this would have to be corrected for in an iterative manner as they are convolved.

One measurement taken by the InSight lander is changes in the length-of-day (LOD) (Folkner et al., 2018; Spiga et al., 2018). There have been previous estimates of this process based on modeling the growth of the SPCs (Karatekin et al., 2006). This process is controlled by changes in the C_{20} gravity coefficient, and thus because our estimates of the change in C_{20} are larger than previous estimates, our estimated variations in LOD are larger, shown in figure 13 We convert the degree two coefficient to the LOD variation through equation 8, modified from Karatekin et al. (2006):

$$\boldsymbol{\Delta \mathrm{LOD} = -LOD\frac{2MR^2}{3C}\Delta C_{20}} \tag{8}$$

Where $\boldsymbol{\frac{C}{MR^2} = 0.365}$ and $\boldsymbol{LOD = 88{,}775s}$. This estimate is just based upon the change in the moment of inertia. Further results from the RISE experiment on InSight will be able to further refine the expectation of LOD variations and perhaps be able to constrain the interior properties of Mars based on the measured value.

Figure 13: LOD variation based on our estimates of the change in C20.

Elastic properties of the lithosphere may change laterally across Mars, as they do on Earth. As previously described, we ignored any lateral variations in elastic properties in our calculations. However, a mission that could detect any differences in measurements of lithospheric deflection laterally would hint at lateral changes in elastic properties. These observations would provide a way to study, for example, differences in the elastic properties across the hemispheric dichotomy.

5 Conclusion

We modeled the expected elastic deformation of the lithosphere of Mars in response to the time-variable load represented by the planet's seasonal ice caps. We showed that the magnitude of this deflection is as high as centimeters and could realistically be measured by a dedicated geodetic instrument. Further modeling of displacements with viscoelastic rheologies would need to be conducted to model the effect of viscous dissipation in the mantle. It is unlikely that this deflection could be detected in current laser and radar altimetry but could realistically be resolved by a future geodetic lander on Mars. A dedicated orbital gravity mission would also be useful in resolving the inter-annual variations of the polar caps. Furthermore, these missions could help deconvolve the CO_2 and dust mass transport processes in already collected time variable gravity data. Observing these displacements presents a relatively low-cost way to constrain the internal mechanical properties of the Martian lithosphere and interior that would have implications for the thermal evolution of the planet. The determination of the LLNs and their contribution to the time variable gravity field of Mars would provide a novel method to reconcile the variety of interior models we currently have for Mars as the LLNs, especially *h'*, are highly sensitive to the interior model. The displacements are not highly sensitive to changes in topography or crustal thickness, however, with high enough precision a suite of geodetic instruments could measure this displacement finely enough to study the effect of lateral changes in the crust on seasonal loading. The methodology established in this study can be used on other planetary bodies, such as Venus and Titan. However, proper consideration must be applied to the loading period of any seasonal deposits or atmospheric transport and consider what time scale they would be measured over.

Acknowledgments

The authors would like to acknowledge the Keck Institute for Space Studies for inspiring this project. N.L.W. would like to acknowledge generous help from Haifeng Xiao and Hilary Martens for help relating to implementing the height variations and using LoadDef. N.L.W would also like to extend thanks to Alexander Berne for testing changes in LLNs and displacements with variable lateral structure.

Open Research

LoadDef can be accessed via this link: https://github.com/hrmartens/LoadDef (Martens et al. 2016). The SPC height variation data can be accessed through https://doi.org/10.17632/z59b9nd6s9.2 (Xiao et al. 2022c) and https://doi.org/10.17632/x953mzxxvv.1 (Xiao et al. 2022b). SHTools can be accessed via https://github.com/SHTOOLS/ (Wieczorek & Meschede 2018). The surface displacements and code to recreate each plot in this paper will be published under the reserved doi on Zenodo: 10.5281/zenodo.7964125 (Wagner et al. 2023). Software and data archiving is still underway.

References

Acton, C., Bachman, N., Semenov, B., & Wright, E. (2018). A look towards the future in the handling of space science mission geometry. *Planetary and Space Science*, *150*, 9–12. https://doi.org/10.1016/j.pss.2017.02.013

Acton, C. H. (1996). *Ancillary data services of NASA's Navigation and Ancillary Information Facility*. *Planet. Space Sci* (Vol. 44).

Agnew, D. C. (2015). Earth tides. *Treatise on Geophysics: Second Edition*, *52*(3), IUGG5–IUGG7. https://doi.org/10.1029/EO052i003pIU005

Aharonson, O., Zuber, M. T., Smith, D. E., Neumann, G. A., Feldman, W. C., & Prettyman, T. H. (2004). Depth, distribution, and density of CO2 deposition on Mars. *Journal of Geophysical Research: Planets*, *109*(5). https://doi.org/10.1029/2003JE002223

Asmar, S. W., Konopliv, A. S., Watkins, M. M., Williams, J. G., Park, R. S., Kruizinga, G., et al. (2014). The scientific measurement system of the gravity recovery and interior laboratory (GRAIL) mission. In *GRAIL: Mapping the Moon's Interior* (Vol. 9781461495840, pp. 25–55). Springer New York. https://doi.org/10.1007/978-1-4614-9584-0_3

Bagheri, A., Khan, A., Al-Attar, D., Crawford, O., & Giardini, D. (2019). Tidal Response of Mars Constrained From Laboratory-Based Viscoelastic Dissipation Models and Geophysical Data. *Journal of Geophysical Research: Planets*, *124*(11), 2703–2727. https://doi.org/10.1029/2019JE006015

Bagheri, Amirhossein, Efroimsky, M., Castillo-Rogez, J., Goossens, S., Plesa, A. C., Rambaux, N., et al. (2022). Tidal insights into rocky and icy bodies: an introduction and overview. *Advances in Geophysics*, *63*, 231–320. https://doi.org/10.1016/bs.agph.2022.07.004

Blewitt, G. (2003). Self-consistency in reference frames, geocenter definition, and surface loading of the solid Earth. *Journal of Geophysical Research: Solid Earth*, *108*(B2). https://doi.org/10.1029/2002jb002082

Briaud, A., Fienga, A., Melini, D., Rambaux, N., Mémin, A., Spada, G., et al. (2023). Constraints on the lunar core viscosity from tidal deformation. *Icarus*, *394*. https://doi.org/10.1016/j.icarus.2023.115426

Broquet, A., Wieczorek, M. A., & Fa, W. (2020). Flexure of the Lithosphere Beneath the North Polar Cap of Mars: Implications for Ice Composition and Heat Flow. *Geophysical Research Letters*, *47*(5), 1–8. https://doi.org/10.1029/2019GL086746

Broquet, A., Wieczorek, M. A., & Fa, W. (2021). The Composition of the South Polar Cap of Mars Derived From Orbital Data. *Journal of Geophysical Research: Planets*, *126*(8). https://doi.org/10.1029/2020JE006730

Drilleau, M., Samuel, H., Rivoldini, A., Panning, M., & Lognonné, P. (2021). Bayesian inversion of the Martian structure using geodynamic constraints. *Geophysical Journal International*, 1615–1644. https://doi.org/10.1093/gji/ggab105

Farrell, W. E. (1972). Deformation of the Earth by surface loads. *Reviews of Geophysics*.

https://doi.org/10.1029/RG010i003p00761

Folkner, W. M., Dehant, V., Le Maistre, S., Yseboodt, M., Rivoldini, A., Van Hoolst, T., et al. (2018). The Rotation and Interior Structure Experiment on the InSight Mission to Mars. *Space Science Reviews*, *214*(5), 1–16. https://doi.org/10.1007/S11214-018-0530-5/TABLES/3

Genova, A., Goossens, S., Lemoine, F. G., Mazarico, E., Neumann, G. A., Smith, D. E., & Zuber, M. T. (2016). Seasonal and static gravity field of Mars from MGS, Mars Odyssey and MRO radio science. *Icarus*, *272*, 228–245. https://doi.org/10.1016/j.icarus.2016.02.050

Van Hoolst, T., Dehant, V., Roosbeek, F., & Lognonné, P. (2003). Tidally induced surface displacements, external potential variations, and gravity variations on Mars. *Icarus*, *161*(2), 281–296. https://doi.org/10.1016/S0019-1035(02)00045-3

Karatekin, Ö., Van Hoolst, T., & Dehant, V. (2006). Martian global-scale CO2 exchange from time-variable gravity measurements. *Journal of Geophysical Research: Planets*, *111*(6). https://doi.org/10.1029/2005JE002591

Khan, A., Liebske, C., Rozel, A., Rivoldini, A., Nimmo, F., Connolly, J. A. D., et al. (2018). A Geophysical Perspective on the Bulk Composition of Mars. *Journal of Geophysical Research: Planets*, *123*(2), 575–611. https://doi.org/10.1002/2017JE005371

Konopliv, A. S., Asmar, S. W., Folkner, W. M., Karatekin, Ö., Nunes, D. C., Smrekar, S. E., et al. (2011). Mars high resolution gravity fields from MRO, Mars seasonal gravity, and other dynamical parameters. *Icarus*, *211*(1), 401–428. https://doi.org/10.1016/j.icarus.2010.10.004

Lemoine, F., Bruinsma, S., Chinn, D., & Forbes, J. (2006). Thermospheric Studies with Mars Global Surveyor. In *AIAA/AAS Astrodynamics Specialist Conference and Exhibit*. American

Institute of Aeronautics and Astronautics. https://doi.org/doi:10.2514/6.2006-6395

Longman, I. M. (1963). *A Green's Function for Determining the Deformation of the Earth under Surface Mass Loads 2. Computations and Numerical Results •. JOURNAL OF GEOPHYSICAL RESEARCH* (Vol. 68).

Love, A. E. H. (1906). *A TREATISE ON THE MATHEMATICAL THEORY OF ELASTICITY* (Second). London: Cambridge City Press.

Love, A. E. H. (1911). *Some Problems of Geodynamics*.

Le Maistre, S., Rivoldini, A., Caldiero, A., Yseboodt, M., Baland, R.-M., Beuthe, M., et al. (2023). Spin state and deep interior structure of Mars from InSight radio tracking. *Nature*. https://doi.org/10.1038/s41586-023-06150-0

Martens, H. R., Rivera, L., Simons, M., & Ito, T. (2016). The sensitivity of surface mass loading displacement response to perturbations in the elastic structure of the crust and mantle. *Journal of Geophysical Research: Solid Earth*, *121*(5), 3911–3938. https://doi.org/10.1002/2015JB012456

Martens, H. R., Rivera, L., & Simons, M. (2019). LoadDef: A Python-Based Toolkit to Model Elastic Deformation Caused by Surface Mass Loading on Spherically Symmetric Bodies. *Earth and Space Science*, *6*(2), 311–323. https://doi.org/10.1029/2018EA000462

McCarthy, D. D., & Petit, G. (2003). *IERS Conventions*.

Métivier, L., Karatekin, Ö., & Dehant, V. (2008). The effect of the internal structure of Mars on its seasonal loading deformations. *Icarus*, *194*(2), 476–486. https://doi.org/10.1016/j.icarus.2007.12.001

Mimoun, D., Murdoch, N., Lognonné, P., Hurst, K., Pike, W. T., Hurley, J., et al. (2017). The Noise Model of the SEIS Seismometer of the InSight Mission to Mars. *Space Science*

Reviews, *211*(1–4), 383–428. https://doi.org/10.1007/S11214-017-0409-X/TABLES/6

Ojha, L., Karimi, S., Lewis, K. W., Smrekar, S. E., & Siegler, M. (2019). Depletion of Heat Producing Elements in the Martian Mantle. *Geophysical Research Letters*, *46*(22), 12756–12763. https://doi.org/10.1029/2019GL085234

Ojha, L., Karimi, S., Buffo, J., Nerozzi, S., Holt, J. W., Smrekar, S., & Chevrier, V. (2021). Martian Mantle Heat Flow Estimate From the Lack of Lithospheric Flexure in the South Pole of Mars: Implications for Planetary Evolution and Basal Melting. *Geophysical Research Letters*, *48*(2), 1–10. https://doi.org/10.1029/2020GL091409

Petricca, F., Genova, A., Goossens, S., Iess, L., & Spada, G. (2022). Constraining the Internal Structures of Venus and Mars from the Gravity Response to Atmospheric Loading. *The Planetary Science Journal*, *3*(7), 164. https://doi.org/10.3847/PSJ/ac7878

Piqueux, S., Kleinböhl, A., Hayne, P. O., Kass, D. M., Schofield, J. T., & McCleese, D. J. (2015). Variability of the martian seasonal CO2 cap extent over eight Mars Years. *Icarus*, *251*, 164–180. https://doi.org/10.1016/J.ICARUS.2014.10.045

Porcelli, L., Tibuzzi, M., Mondaini, C., Salvatori, L., Muccino, M., Petrassi, M., et al. (2019, January 1). Optical-Performance Testing of the Laser RetroReflector for InSight. *Space Science Reviews*. Springer Netherlands. https://doi.org/10.1007/s11214-018-0569-3

Rietbroek, R., Fritsche, M., Dahle, C., Brunnabend, S. E., Behnisch, M., Kusche, J., et al. (2014). Can GPS-Derived Surface Loading Bridge a GRACE Mission Gap? *Surveys in Geophysics*, *35*(6), 1267–1283. https://doi.org/10.1007/s10712-013-9276-5

Samuel, H., Lognonné, P., Panning, M., & Lainey, V. (2019). The rheology and thermal history of Mars revealed by the orbital evolution of Phobos. *Nature*, *569*(7757), 523–527. https://doi.org/10.1038/s41586-019-1202-7

Smith, D. E., Zuber, M. T., & Neumann, G. A. (2001). Seasonal variations of snow depth on mars. *Science*, *294*(5549), 2141–2146. https://doi.org/10.1126/science.1066556

Smith, David E., Zuber, M. T., Torrence, M. H., Dunn, P. J., Neumann, G. A., Lemoine, F. G., & Fricke, S. K. (2009). Time variations of Mars' gravitational field and seasonal changes in the masses of the polar ice caps. *Journal of Geophysical Research E: Planets*, *114*(5), 1–15. https://doi.org/10.1029/2008JE003267

Sori, M., Ermakov, A. I., Keane, J. T., Bierson, C. J., Bills, B. G., Bramson, A. M., et al. (2022). COMPELLING SCIENCE ENABLED BY GRAVITY INVESTIGATIONS AT MARS. M.

Sori, M. M., Keane, J. T., & Ermakov, A. I. (2023). *Next Generation Planetary Geodesy*. Pasadena, CA. https://doi.org/10.7907/y1m4-ek67

Spiga, A., Banfield, D., Teanby, N. A., Forget, F., Lucas, A., Kenda, B., et al. (2018). Atmospheric Science with InSight. *Space Science Reviews*, *214*(7), 1–64. https://doi.org/10.1007/S11214-018-0543-0/FIGURES/19

Stähler, S. C., Khan, A., Banerdt, W. B., Lognonné, P., Ceylan, S., Drilleau, M., et al. (2021). Seismic detection of the Martian core. *Science*, *448*(July), 443–448.

Steinbrügge, G., Stark, A., Hussmann, H., Sohl, F., & Oberst, J. (2015). Measuring tidal deformations by laser altimetry. A performance model for the Ganymede Laser Altimeter. *Planetary and Space Science*, *117*, 184–191. https://doi.org/10.1016/j.pss.2015.06.013

Takeuchi, H. (1950). *ON THE EARTH TIDE OF THE COMPRESSIBLE EARTH OF VARIABLE DENSITY AND ELASTICITY* (Vol. 31).

Wieczorek, M. A. (2015). *Gravity and Topography of the Terrestrial Planets*. *Treatise on Geophysics: Second Edition* (Vol. 10). https://doi.org/10.1016/B978-0-444-53802-4.00169-X

Wieczorek, Mark A., & Meschede, M. (2018). SHTools: Tools for Working with Spherical Harmonics. *Geochemistry, Geophysics, Geosystems*, *19*(8), 2574–2592. https://doi.org/10.1029/2018GC007529

Williams, J. G., Boggs, D. H., Yoder, C. F., Ratcliff, J. T., & Dickey, J. O. (2001). Lunar rotational dissipation in solid body and molten core. *Journal of Geophysical Research: Planets*, *106*(E11), 27933–27968. https://doi.org/10.1029/2000JE001396

Williams, J. G., Turyshev, S. G., Boggs, D. H., & Ratcliff, J. T. (2006). Lunar laser ranging science: Gravitational physics and lunar interior and geodesy. In *Advances in Space Research* (Vol. 37, pp. 67–71). Elsevier Ltd. https://doi.org/10.1016/j.asr.2005.05.013

Xiao, H., Stark, A., Steinbrügge, G., Thor, R., Schmidt, F., & Oberst, J. (2022). Prospects for mapping temporal height variations of the seasonal CO2 snow/ice caps at the Martian poles by co-registration of MOLA profiles. *Planetary and Space Science*, *214*. https://doi.org/10.1016/j.pss.2022.105446

Xiao, H., Stark, A., Schmidt, F., Hao, J., Steinbrügge, G., Wagner, N. L., et al. (2022). Spatio-Temporal Level Variations of the Martian Seasonal North Polar Cap From Co-Registration of MOLA Profiles. *Journal of Geophysical Research: Planets*, *127*(10), e2021JE007158. https://doi.org/10.1029/2021JE007158

Xiao, H., Stark, A., Schmidt, F., Hao, J., Su, S., Steinbrügge, G., & Oberst, J. (2022). Spatio-Temporal Level Variations of the Martian Seasonal South Polar Cap From Co-Registration of MOLA Profiles. *Journal of Geophysical Research: Planets*, *127*(7). https://doi.org/10.1029/2022JE007196

Figure 1.

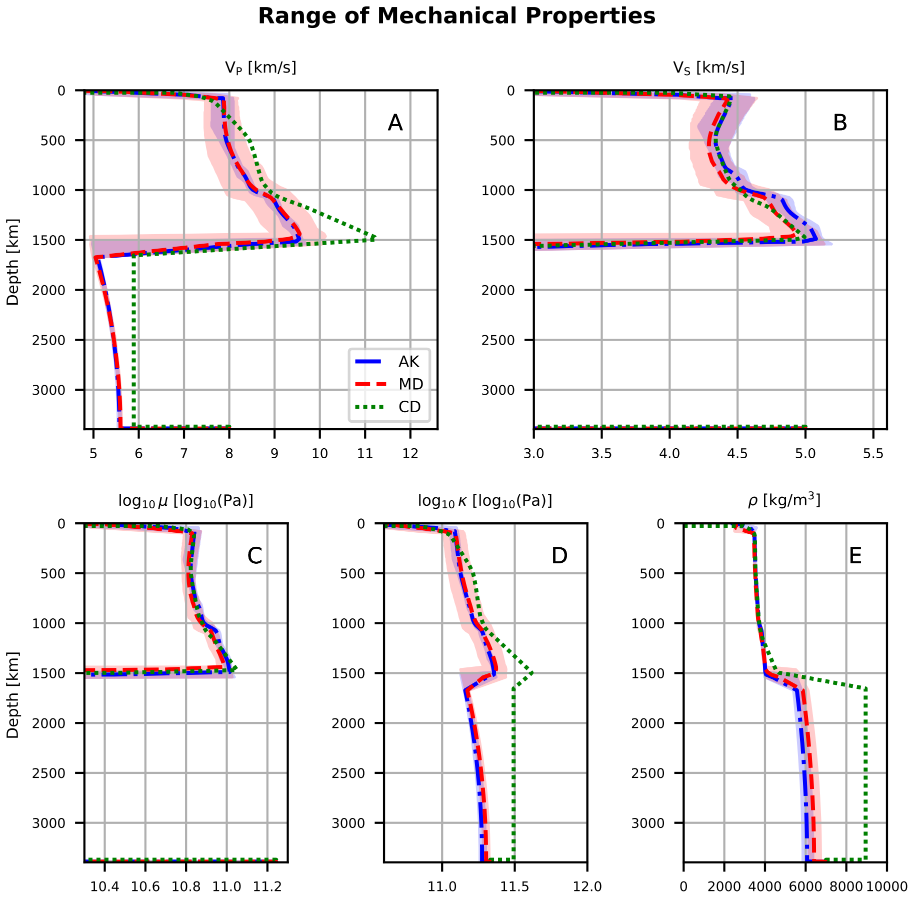

Range of Mechanical Properties
V_P [km/s]
V_S [km/s]
Depth [km]
A
B
C
D
E
AK
MD
CD
log10 μ [log10(Pa)]
log10 κ [log10(Pa)]
ρ [kg/m3]

Figure 2.

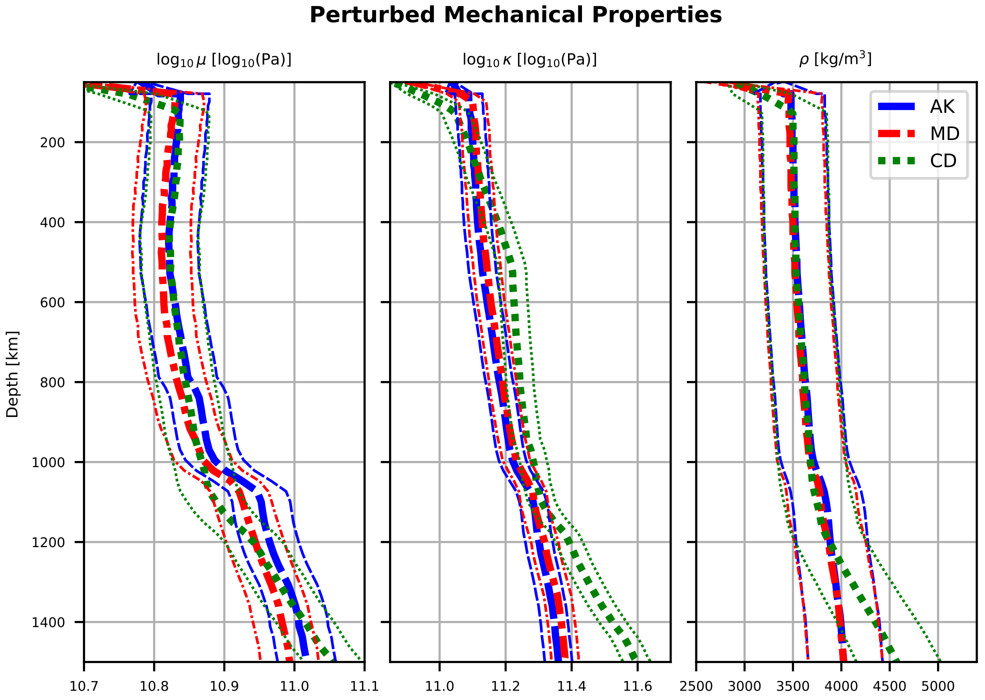

Perturbed Mechanical Properties
$\log_{10}\mu$ [$\log_{10}$(Pa)]
$\log_{10}\kappa$ [$\log_{10}$(Pa)]
ρ [kg/m^3]
Depth [km]
200
400
600
800
1000
1200
1400
10.7
10.8
10.9
11.0
11.1
11.0
11.2
11.4
11.6
2500
3000
3500
4000
4500
5000
AK
MD
CD

Figure 3.

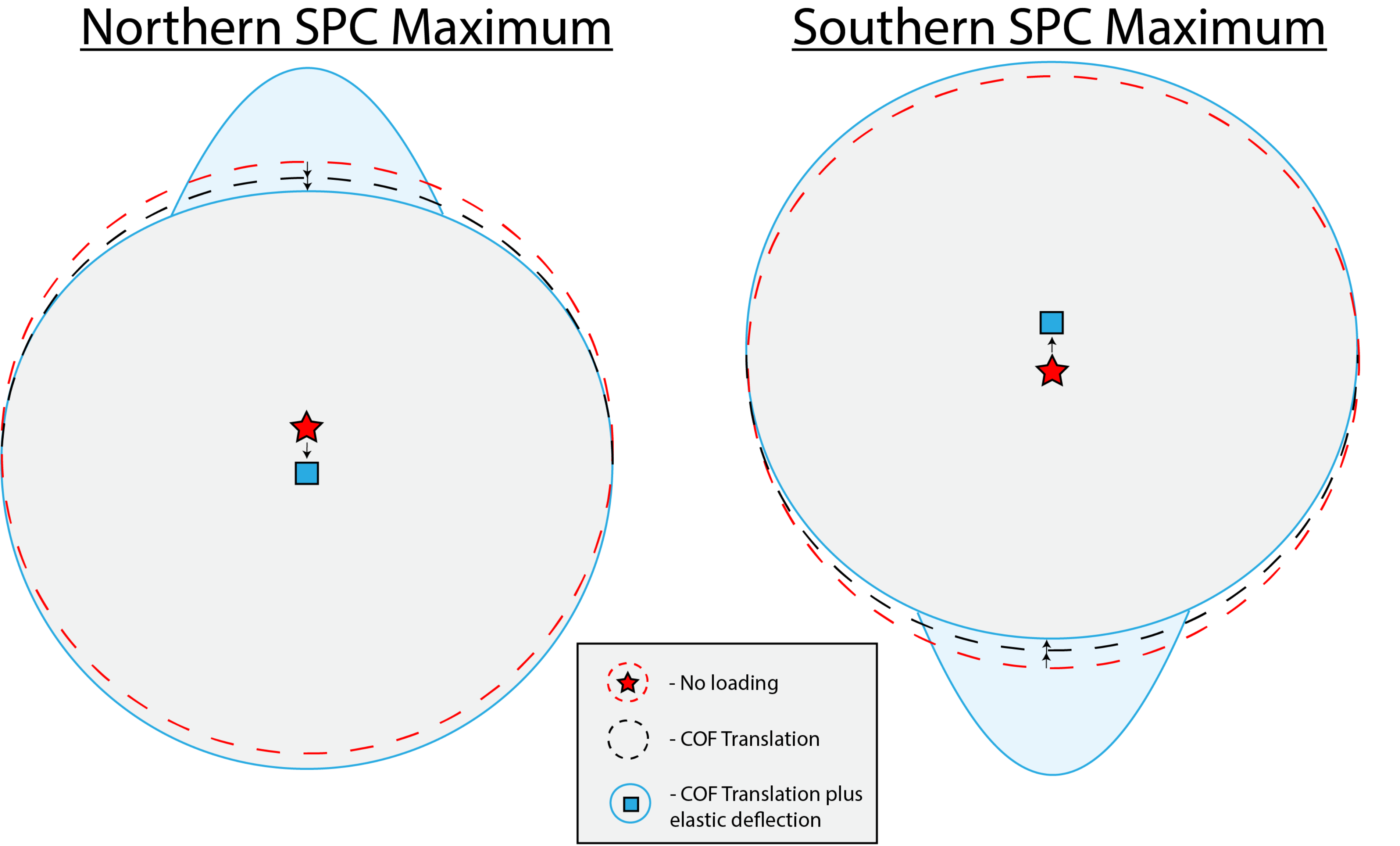

Northern SPC Maximum
Southern SPC Maximum
- No loading
- COF Translation
- COF Translation plus elastic deflection

Figure 4.

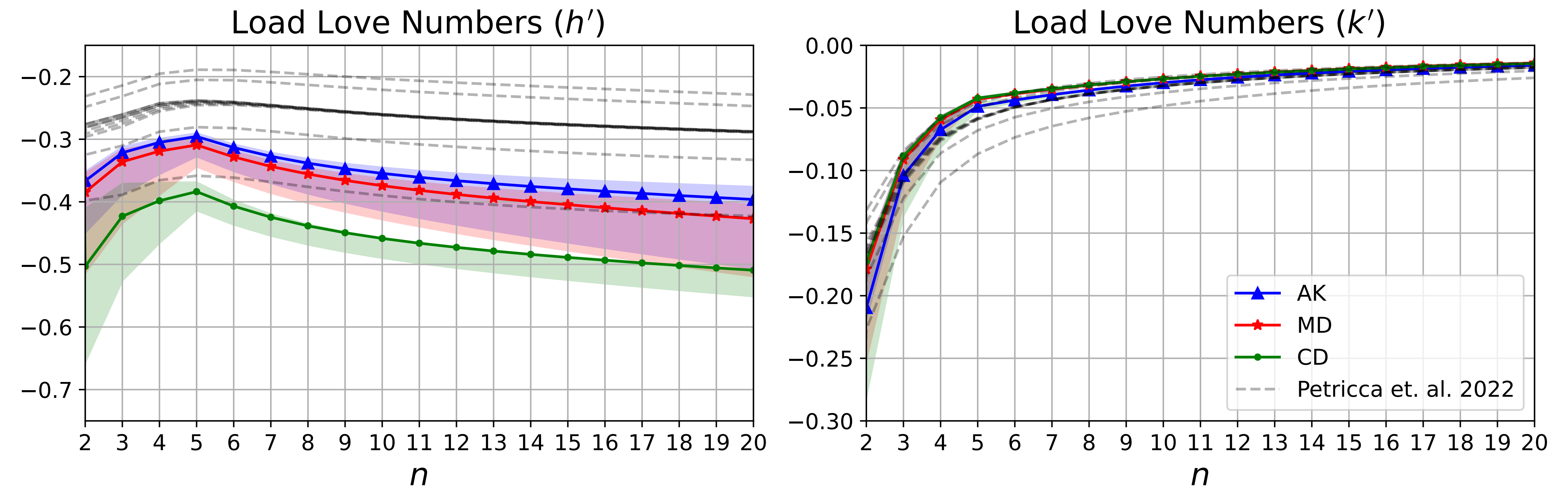
Load Love Numbers (h')
Load Love Numbers (k')
n
n
AK
MD
CD
Petricca et. al. 2022

Figure 5.

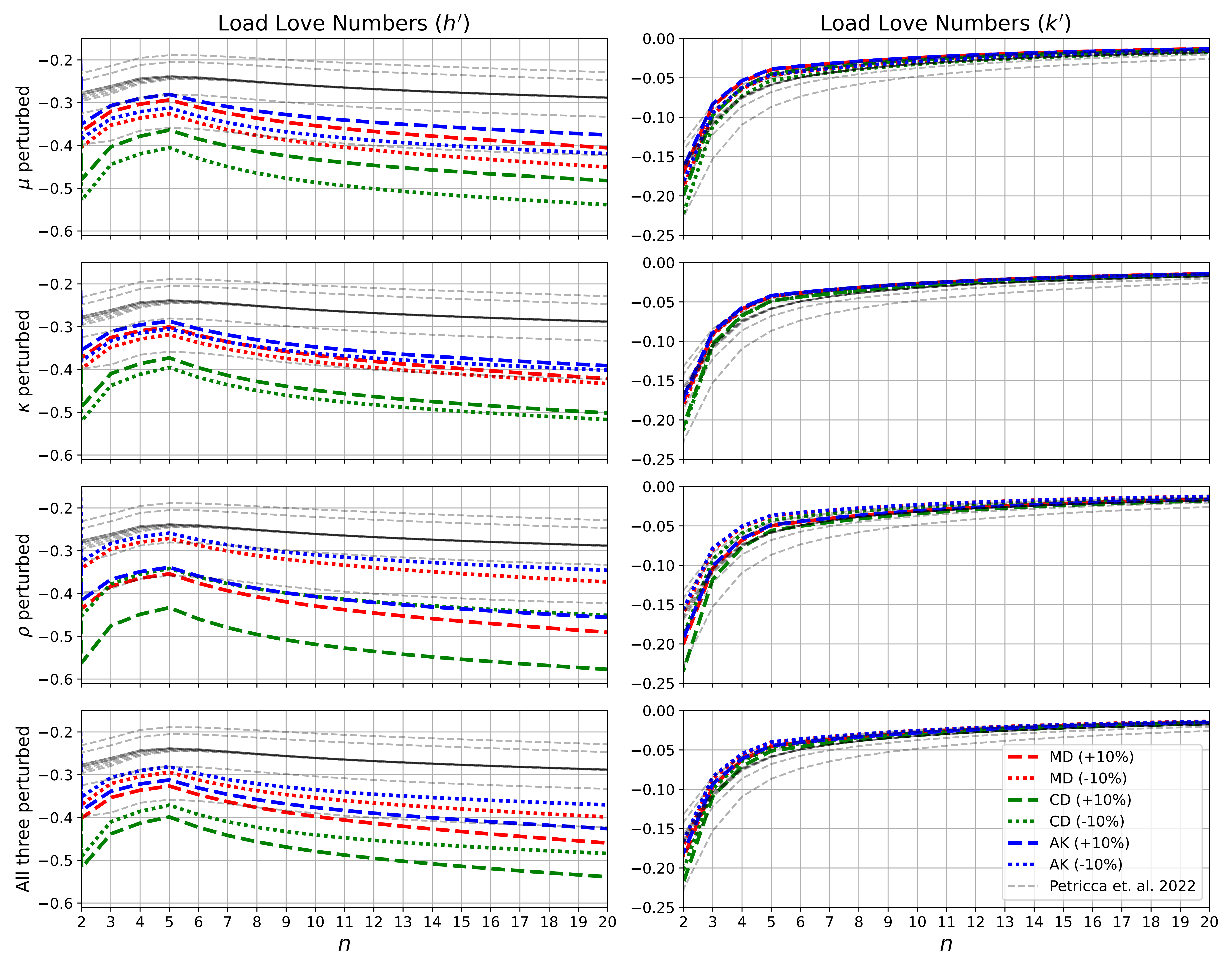

Load Love Numbers (h')
Load Love Numbers (k')
μ perturbed
κ perturbed
ρ perturbed
All three perturbed
n
n
MD (+10%)
MD (-10%)
CD (+10%)
CD (-10%)
AK (+10%)
AK (-10%)
Petricca et. al. 2022

Figure 6.

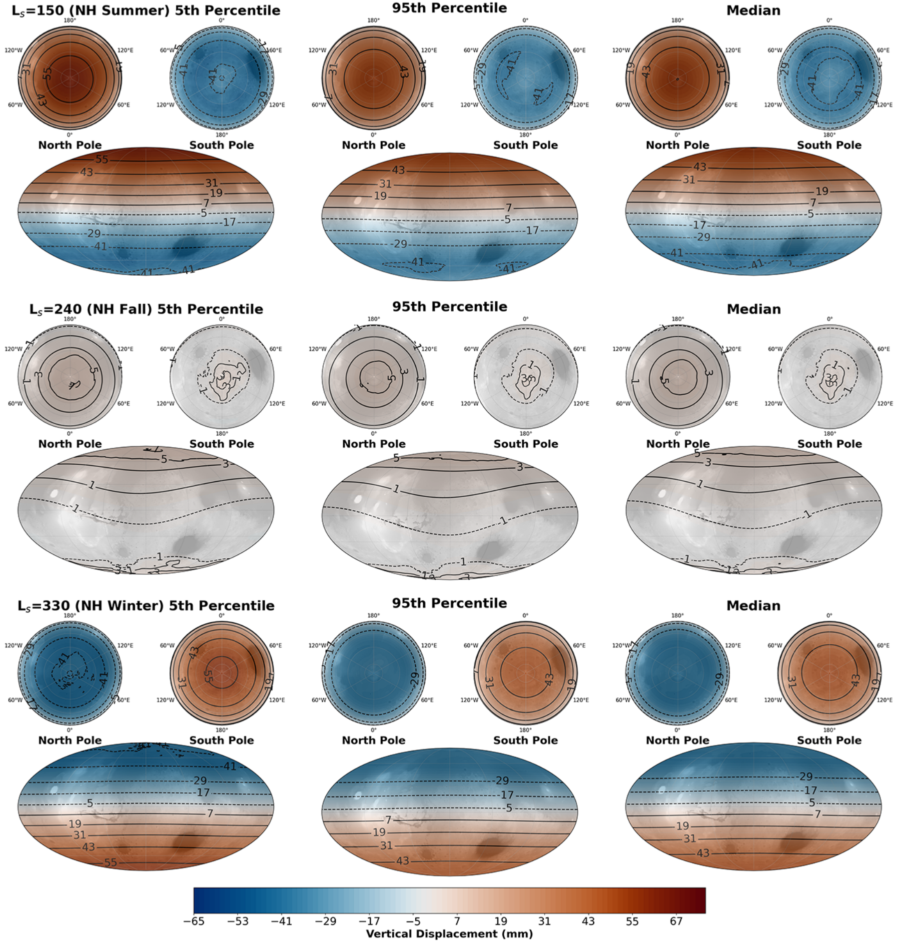

L_S=150 (NH Summer) 5th Percentile
95th Percentile
Median
North Pole
South Pole
L_S=240 (NH Fall) 5th Percentile
95th Percentile
Median
L_S=330 (NH Winter) 5th Percentile
95th Percentile
Median
−65 −53 −41 −29 −17 −5 7 19 31 43 55 67
Vertical Displacement (mm)

Figure 7.

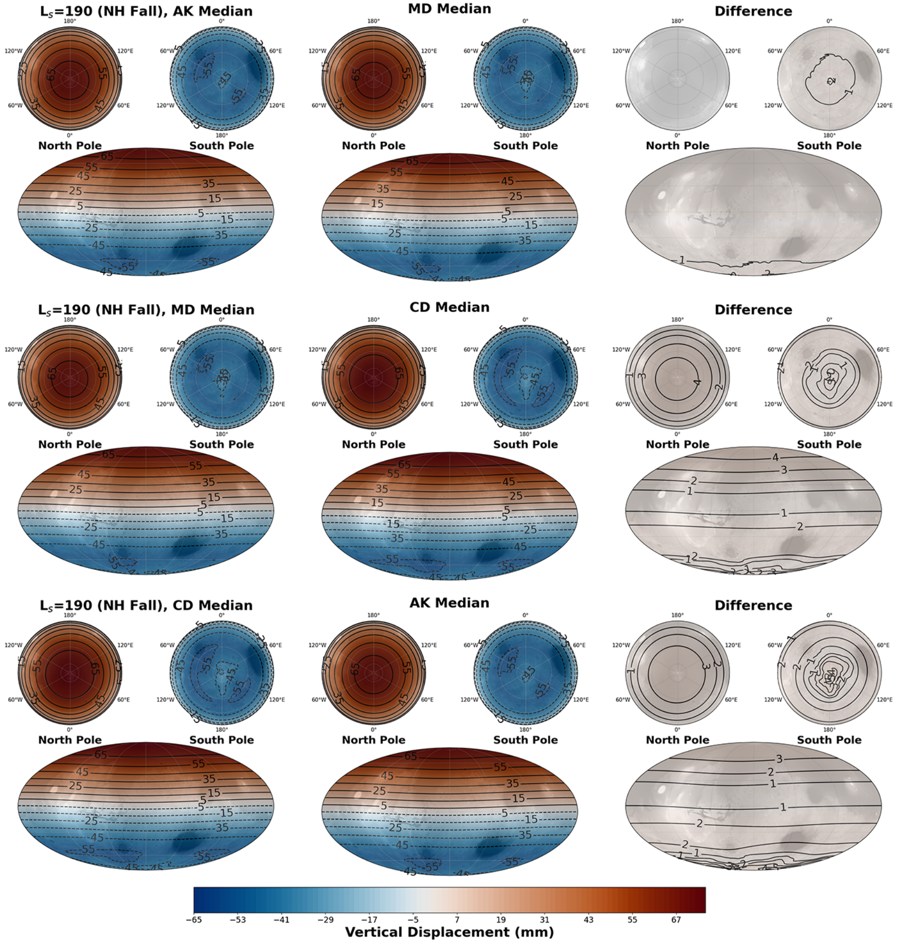

L$_S$=190 (NH Fall), AK Median
MD Median
Difference
L$_S$=190 (NH Fall), MD Median
CD Median
Difference
L$_S$=190 (NH Fall), CD Median
AK Median
Difference
North Pole
South Pole
−65 −53 −41 −29 −17 −5 7 19 31 43 55 67
Vertical Displacement (mm)

Figure 8.

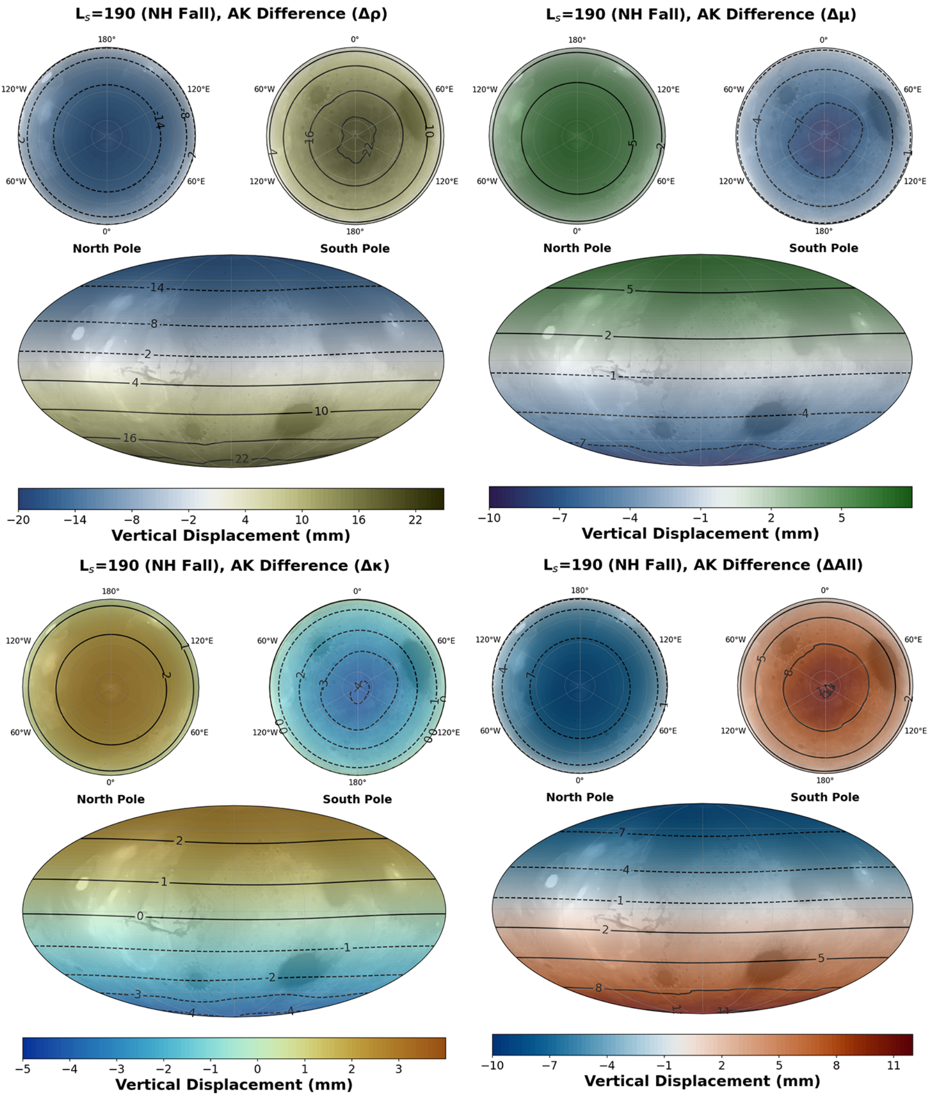

Ls=190 (NH Fall), AK Difference (Δρ)
North Pole
South Pole
−20 −14 −8 −2 4 10 16 22
Vertical Displacement (mm)
Ls=190 (NH Fall), AK Difference (Δμ)
North Pole
South Pole
−10 −7 −4 −1 2 5
Vertical Displacement (mm)
Ls=190 (NH Fall), AK Difference (Δκ)
North Pole
South Pole
−5 −4 −3 −2 −1 0 1 2 3
Vertical Displacement (mm)
Ls=190 (NH Fall), AK Difference (ΔAll)
North Pole
South Pole
−10 −7 −4 −1 2 5 8 11
Vertical Displacement (mm)

Figure 9.

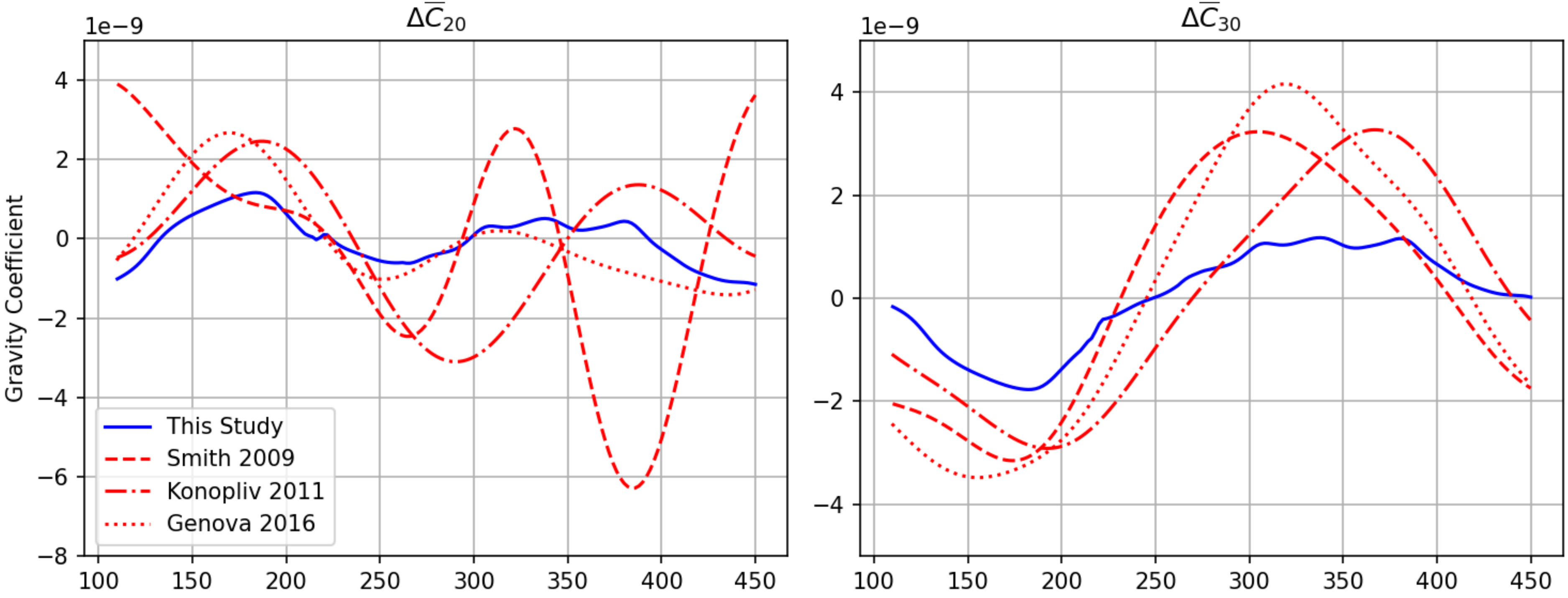

$\Delta\overline{C}_{20}$
1e−9
4
2
0
−2
−4
−6
−8
Gravity Coefficient
This Study
Smith 2009
Konopliv 2011
Genova 2016
100
150
200
250
300
350
400
450
$\Delta\overline{C}_{30}$
1e−9
4
2
0
−2
−4
100
150
200
250
300
350
400
450

Figure 10.

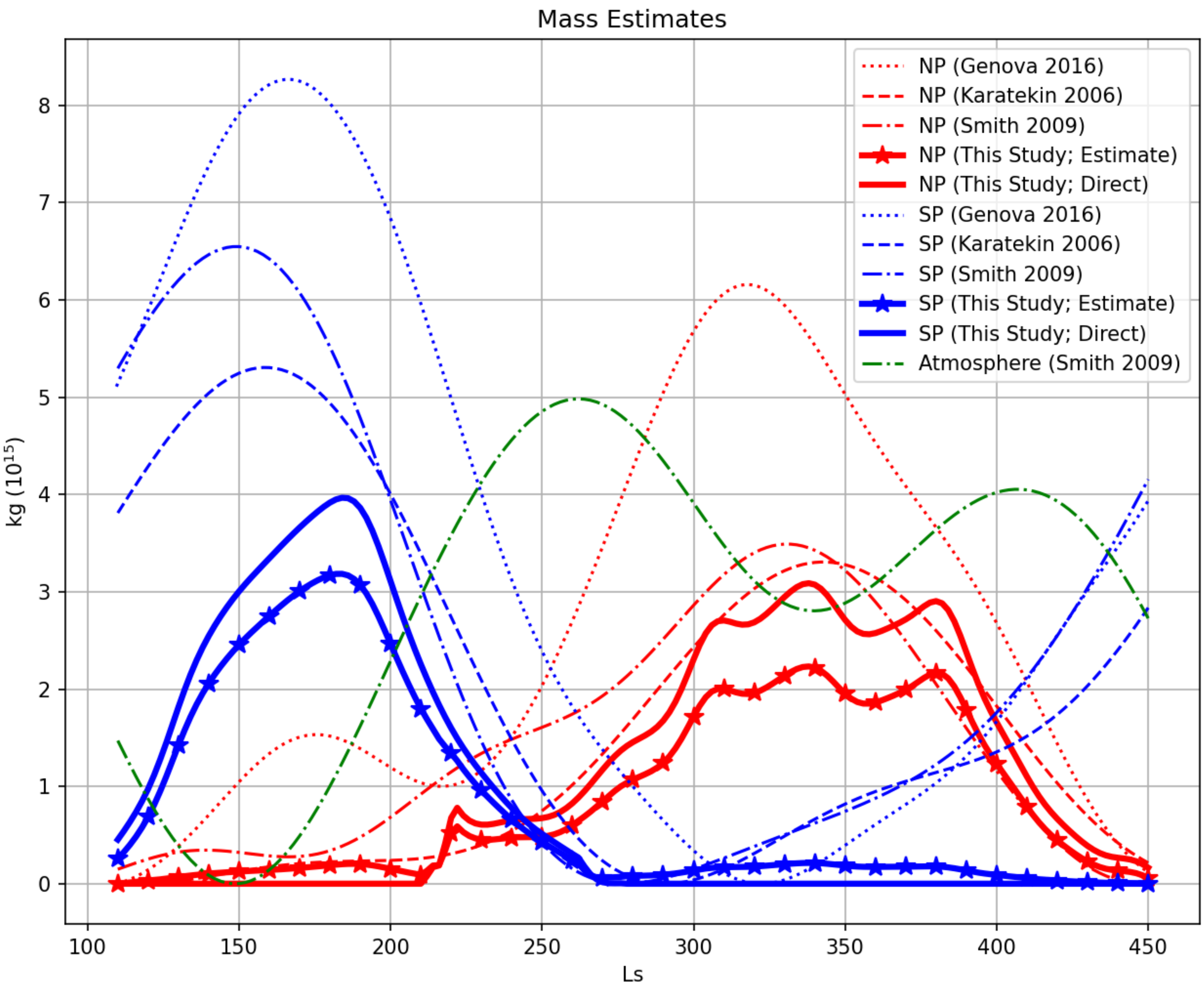

Mass Estimates
NP (Genova 2016)
NP (Karatekin 2006)
NP (Smith 2009)
NP (This Study; Estimate)
NP (This Study; Direct)
SP (Genova 2016)
SP (Karatekin 2006)
SP (Smith 2009)
SP (This Study; Estimate)
SP (This Study; Direct)
Atmosphere (Smith 2009)
kg (10^{15})
Ls
0
1
2
3
4
5
6
7
8
100
150
200
250
300
350
400
450

Figure 11.

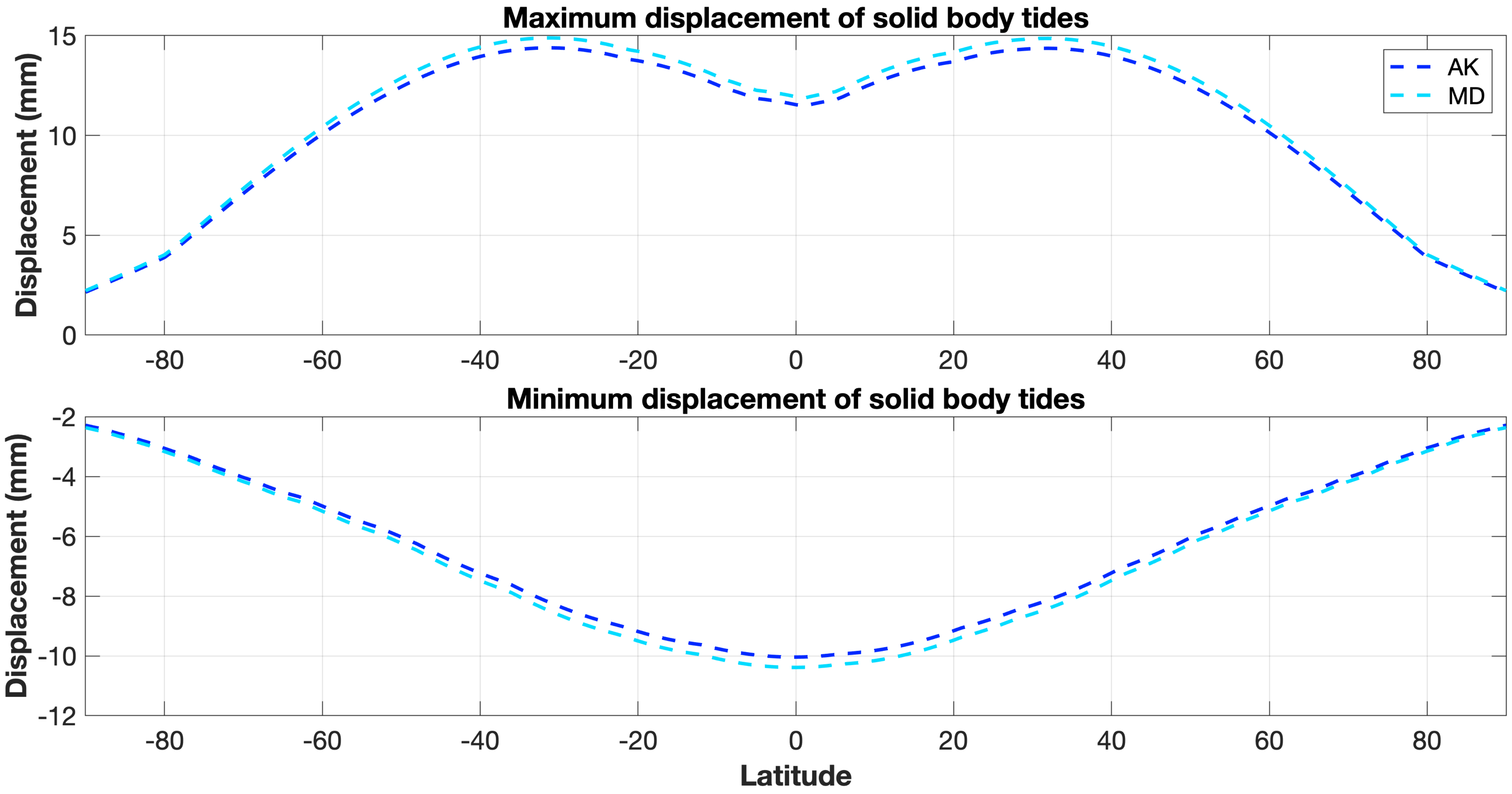

Maximum displacement of solid body tides
Displacement (mm)
15
10
5
0
-80
-60
-40
-20
0
20
40
60
80
AK
MD
Minimum displacement of solid body tides
Displacement (mm)
-2
-4
-6
-8
-10
-12
-80
-60
-40
-20
0
20
40
60
80
Latitude

Figure 12.

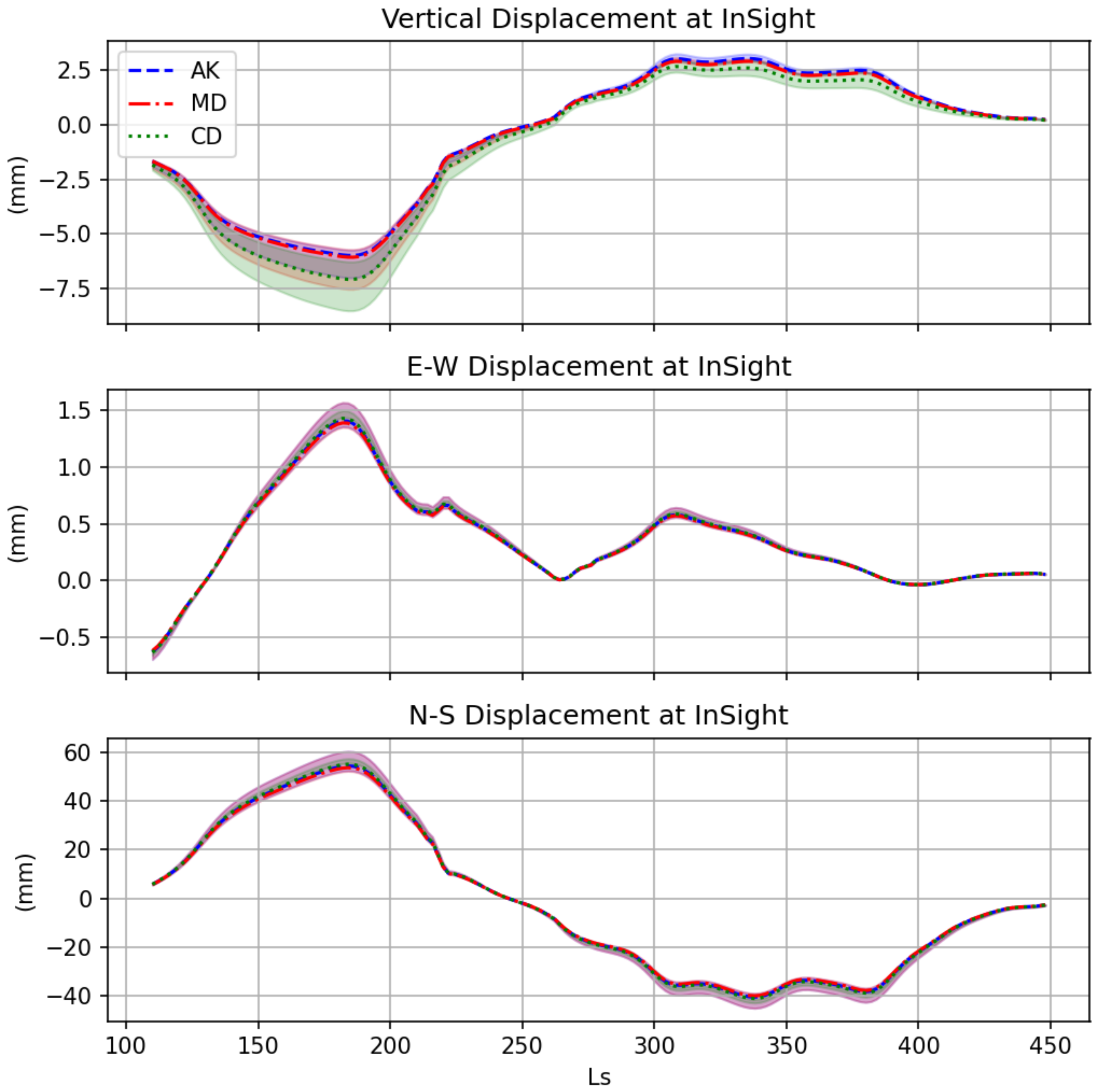
Vertical Displacement at InSight
AK
MD
CD
(mm)
2.5
0.0
−2.5
−5.0
−7.5
E-W Displacement at InSight
(mm)
1.5
1.0
0.5
0.0
−0.5
N-S Displacement at InSight
(mm)
60
40
20
0
−20
−40
100
150
200
250
300
350
400
450
Ls

Figure 13.

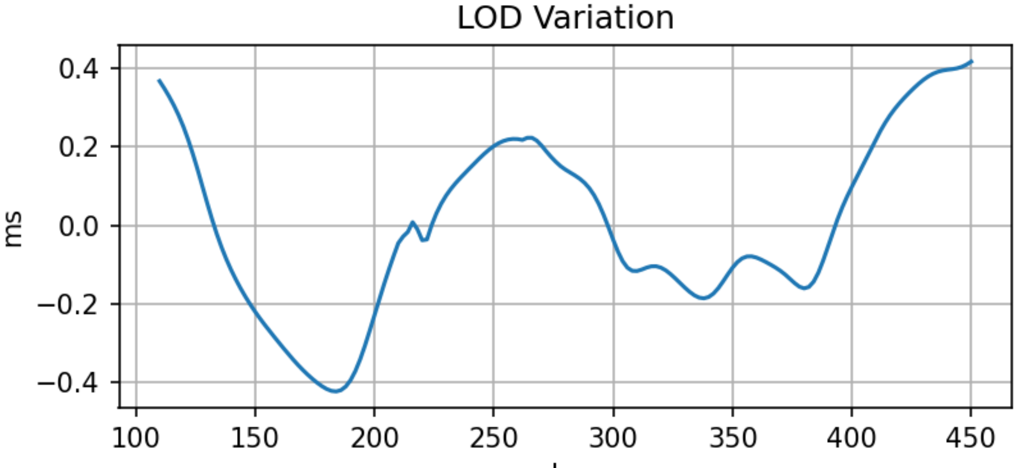
LOD Variation
ms
0.4
0.2
0.0
−0.2
−0.4
100
150
200
250
300
350
400
450